Statistics of Velocity Field in Laboratory-Simulated Downburst

Taiichi Nagata*
Japan Aerospace Exploration Agency, Tsukuba 305-8505, Japan
and
Shinnosuke Obi[†] and Shigeaki Masuda[†]
Keio University, Yokohama 223-8522, Japan

As a laboratory model of downburst, the statistics of a turbulent velocity field of a vertical gravitational flow is investigated. By mechanically breaking a thin film fixed at the bottom of a cylindrical container, a finite mass of a high-density liquid begins to fall into a stationary low-density liquid, forming a vertical thermal. It impinges onto the horizontal ground and then diverges radially outward. By employing particle image velocimetry, the ensemble-averaged maps of velocity vectors, azimuthal vorticity, and turbulent stresses in a meridian plane are obtained. The statistical characteristics in the downdraft stage, impinging stage and diverging stage are examined. The nature and the role of the circulatory flow are demonstrated. The results show reasonable agreement with the actual downbursts observed in the atmosphere. Based on these results, the windshear hazard index for aircraft encountering a downburst is evaluated.

Nomenclature

a	=	radius of spherical vortex
C	=	numerical constant
g	=	gravitational acceleration
h	=	approaching altitude
k	=	vertical unit vector
P_{zz}, P_{rr}, p_{rz}	=	production rate of Reynolds stress by mean shear
p	=	pressure
p_B	=	buoyancy-driven pressure
p_0	=	pressure at infinity
R_D	=	radius of downdraft column
R_0	=	reference length
Re	=	Reynolds number
T_0	=	reference time
t	=	time after impingement
$\tilde{t}$	=	time after release
t_0	=	center-crossing time
u	=	velocity vector
V_a	=	airspeed relative to aircraft
V_g	=	ground speed
V_r	=	ensemble-averaged radial velocity
V_z	=	ensemble-averaged vertical velocity
V_0	=	reference velocity
$\overline{v_z^2}, \overline{v_r^2}, \overline{v_z v_r}$	=	Reynolds stress components
μ_0	=	liquid viscosity
ρ	=	liquid density
ρ_0	=	density of ambient low-density liquid
ρ'	=	density fluctuation
$\Delta\rho$	=	initial density difference between two liquids
τ	=	time from t_0
ψ	=	stream function
ω_θ	=	azimuthal component of ensemble-averaged vorticity

I. Introduction

DOWNBURST is a kind of mesoscale meteorological phenomenon in which a mass of cooled midair forms a downdraft, collides with the ground, and turns into a horizontally diverging flow [1]. The associated strong gust often causes aircraft disasters during takeoff and landing. Besides the forecast of its outbreak, knowledge of the statistical characteristics of the velocity field is necessary to prevent or to minimize damage. The time change of velocity during impingement and thereafter is particularly important for designing a safe maneuvering system. Well over 200 samples of downburst have been accumulated through atmospheric observation programs such as NIMROD and JAWS, and its overall feature is now becoming clear [2–6]. However, information on the statistical characteristics of the velocity field is not yet sufficient because of the limitations of both spatial resolution and the number of samples.

As an alternative method, a laboratory simulation was first reported by Lundgren et al. [7], in which water vapor was ignored and a high-density liquid was released into a stationary low-density ambient. Their flow visualization picture showed changes of the outline of the descending parcel and a vortex-ring-like structure in front of the horizontally diverging flow, as well as their convection velocity. Although comparison of global characteristics such as spreading rate of surface outflow with real microburst showed moderate agreement, they did not provide any information on their velocity field. Alahyari and Longmire [8] measured the instantaneous velocity by particle image velocimetry (PIV) at a Reynolds number of 3600 and found a vortex-ring-like structure surrounding the descending parcel in their instantaneous velocity maps.

Srivastava [9] and Proctor [10] reported numerical simulations mainly aimed at the entire life cycle of downburst from outbreak to extinction, while Droegemeier and Wilhelmson [11] and Anderson et al. [12] reported the outbreak and growth of downdraft. Multiple factors such as precipitation, phase change, and heat transfer were incorporated and rather crude assumptions were included. Although the global features were compared with the real observations, the velocity field close to the ground, which is of particular importance for ground structures and aircraft safety, was not resolved sufficiently. Downdraft is closely related to a thermal in

*Engineer, Institute of Aerospace Technology, Tsukuba Space Center, 2-1-1 Sengen.
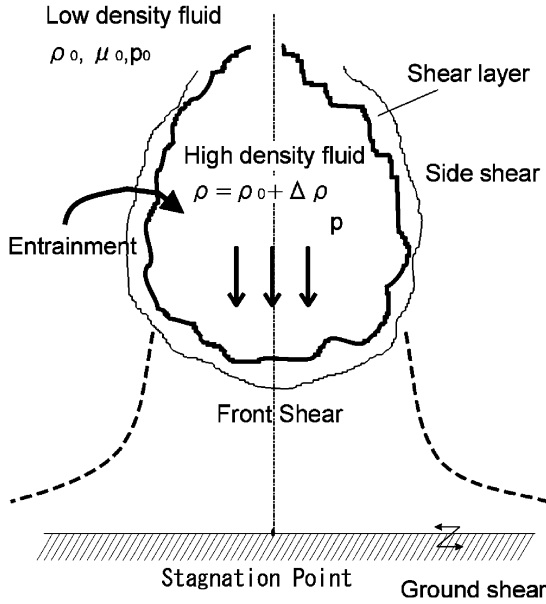†Professor, Department of Mechanical Engineering, Hiyoshi 3-14-1, Kohoku-ku.

Fig. 1   Schematic diagram of flow field.

Fig. 2   Experimental facilities.

which a finite mass of low-density fluid moves upward driven by buoyancy. The primary interests of past investigations lay in the overall shape, moving velocity and entrainment [13–15], and the velocities inside and outside the thermal have not been studied in detail.

In the present study, the statistical behavior of velocity field near the ground is investigated experimentally, assuming that microphysical and thermodynamical effects are not of primary importance. As illustrated in Fig. 1, a finite mass of liquid of slightly higher density $\rho_0 + \Delta\rho$ is released into an ambient liquid of lower density ρ_0 and viscosity μ_0. It forms a vertical inverse thermal followed by a wake. At the front and the side of the thermal, shear layers are formed, which may contribute to turbulence generation. After impinging onto the ground, it diverges radially outward, forms a boundary layer along the ground, and eventually decays due to ground shear.

Assuming incompressibility, a small density difference and uniform viscosity, the Navier–Stokes equation is approximated by

$$\frac{D\boldsymbol{u}}{Dt} = -\frac{1}{\rho_0}\nabla(p - p_0) - \frac{\rho - \rho_0}{\rho_0}g\boldsymbol{k} + \frac{\mu_0}{\rho_0}\nabla^2\boldsymbol{u} \qquad (1)$$

where $\boldsymbol{k}$ is directed upward and p_0 is the pressure in the environment where the fluid is in a hydrostatically balanced reference state. The second term on the right-hand side is the driving force of negative buoyancy. If it is assumed to be of the same order as the convection term, the reference time should be

$$T_0 = \left(\frac{R_0\rho_0}{g\Delta\rho}\right)^{1/2} \qquad (2)$$

The corresponding vorticity equation contains the buoyant production of vorticity $-g(\nabla\rho/\rho) \times \boldsymbol{k}$ which may affect the evolution of the azimuthal vorticity. R_0 is defined as the radius of an equivalent sphere of the same volume as the high-density liquid [7], and the reference velocity is defined as $V_0 = R_0/T_0$. Then the present problem can be specified by Reynolds number $Re \equiv \rho_0 R_0 V_0/\mu_0$ only. It is of the order of 10^3, which is much smaller than that of a real downburst but the large-scale motion is considered to be inviscid, similar to that in the real atmosphere.

II.   Experimental Facility and Methods

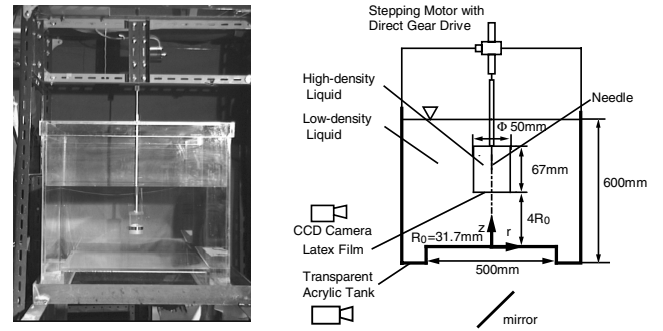The schematic diagram of the experimental apparatus is given in Fig. 2. A tank of $600 \times 600 \times 600$ mm^3, made of transparent acrylic plate, is filled with water solution of glycerol as the low-density ambient liquid. Beneath the free surface, a cylindrical container of 50 mm diameter and 67 mm height is fixed, the bottom of which is closed by latex film 0.1 mm thick. The top is opened to the ambient liquid in order to maintain hydrostatic equilibrium. As the high-density liquid, a water solution of potassium-phosphate is filled into the container. It was employed in order to match its refractive index to that of the ambient liquid, enabling visual studies [8]. By mechanically breaking the film using a needle driven by a stepping motor, the finite mass of high-density liquid begins to fall due to gravity and impinges onto the horizontal plate. R_0 is kept constant at 31.7 mm. Most of the measurements are performed at $Re = 2070$ and $T_0 = 0.45$ s with the initial release height of $4R_0$.

The high-speed video frames showed that, after the moment of burst, the center hole suddenly develops and splits horizontally. The bottom is fully opened after 0.6 ms and the edge of the broken latex film is wound up along the side of the container after 1.1 ms. Despite this, the high-density liquid maintains its bottom shape from just before the moment of burst. For ensemble averaging, these initial events should be repeated under as constant conditions as possible. This is partly accomplished by pretensioning the latex film by applying a constant radial load during mounting. Before the main body of the high-density liquid begins to fall, a sideways movement of the high-density liquid is observed. However, it is assumed not to affect the subsequent development. A trench is prepared around the periphery of the bottom of the tank for draining the high-density liquid after divergence, to enable repeated experimentation.

Reynolds number is varied between 318 and 2100 by changing the weight percent of glycerol and potassium phosphate. The initial density difference $\Delta\rho/\rho_0$ lies in the range of 3×10^{-4} to 160×10^{-4}. A float-type density meter is employed for density measurements. Since the ratio of the viscosities of the two liquids ranges from 0.96 to 1.02, viscosity is assumed to be constant at μ_0.

Velocity data are obtained by a PIV, as illustrated in Fig. 3. Tracer particles (nylon 12, mean diameter 90 μm, specific gravity 1.02) are mixed uniformly into the whole flow field and illuminated by a strobe light sheet of 5 mm thickness to obtain a meridian view. The light is emitted alternatively from two xenon lamps. The timing of illumination is controlled by employing the delay generator to match the even and odd fields of the NTSC-CCD camera (SONY DX-55), and two successive images of the cloud of particles are recorded from the side at a 16.7 ms interval. The images are digitized by employing the frame grabber (National Instrument PCI-IMAQ-1408) with 640×480 pixels and 256 gray scale and stored in the hard disk.

The instantaneous velocity components in r and z directions are then evaluated by the cross-correlation method for pattern matching. The size of the investigation matrix is 19×19 pixels and that of the correlation matrix is 10×10 pixels. The spatial resolution of the optical system is 0.295 mm/pixel and the time resolution is 16.7 ms. A subpixel interpolation algorithm is incorporated in order to improve the spatial resolution. When the absolute value of estimated velocity exceeds the mean value over 8 adjacent areas by 60%, the vector is judged to be erroneous and is rejected. The resulting spatial resolution in total is 0.295 mm/pixel and the uncertainty of velocity measurements is within 5%. Because of the optical constraint, the data point nearest to the ground surface is about 2.9 mm.
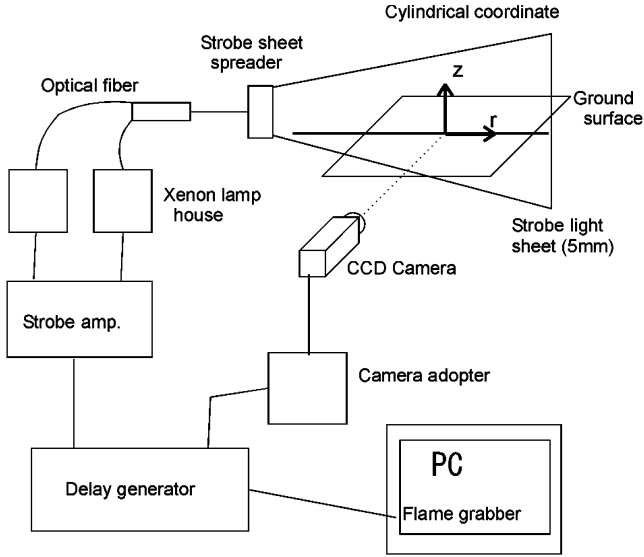
Fig. 3 PIV system and pulse sequence.

Fig. 4 Typical time series of dye visualization pictures ($Re = 625$) (1st and 2nd rows: side view, 3rd row: bottom view).
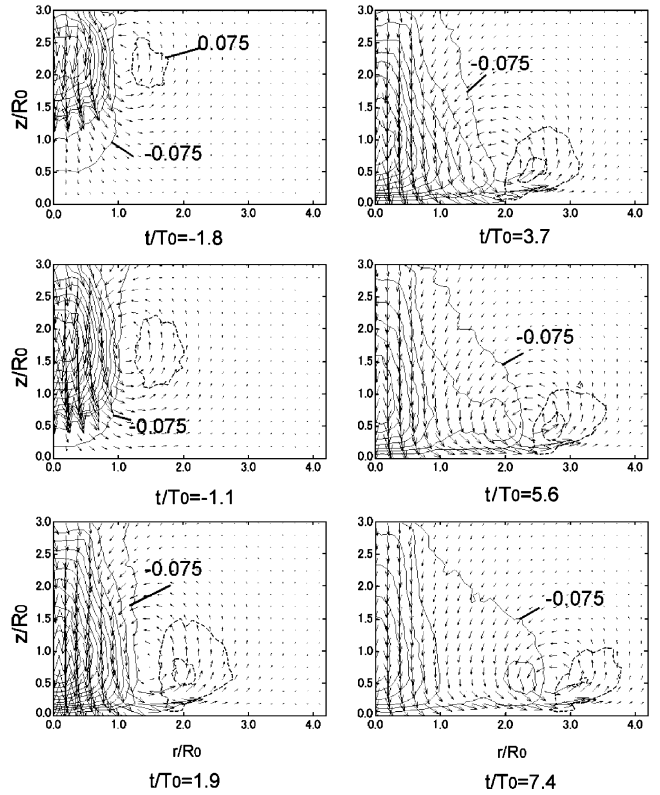

Fig. 5 Ensemble-averaged contours of vertical velocity component together with velocity vector map ($Re = 2100$, contour interval is 0.075, solid and dotted lines indicate negative and positive values).

On the bases of these velocity data, the ensemble-averaged maps of velocity vectors, azimuthal vorticity and Reynolds stress components in the meridian plane are reconstructed. The average is taken over 100 samples, keeping the initial conditions as constant as possible.

III. Measured Results and Discussion

A. Flow Visualization

Figure 4 shows a typical time series of the dye visualization images at $Re = 625$. The dye (Phloxine) is premixed into the high-density liquid. t is normalized by T_0. The moment of impingement will be defined later. After release, the high-density liquid begins to fall due to gravity and forms a thermal. It gradually expands laterally and forms a varicoselike structure which is commonly observed at the top of a plume ($t < 0$). After impingement ($t > 0$), the high-density liquid diverges horizontally outward and forms a vortex-ring-like structure at its front. As seen in the bottom views, the front of the diverging flow exhibits circumferential nonuniformity similar to the Widnall instability of a vortex ring [16]. Since this asymmetry is not repeatable, the ensemble-averaged flow field can be considered to be axially symmetric. With increasing Reynolds number, these structures become finer and more random. The vertical column of dye above the thermal is the trailing flow following the main body of the descending parcel.

B. Mean Velocity Field

The ensemble-averaged contours of the vertical velocity component together with the velocity vector map is given in Fig. 5 for Reynolds number 2100. Assuming axisymmetry, only half of the meridian plane is shown. Because of the limitation of PIV, data is available only in the region $z \geq 0.09R_0$ (≈ 2.9 mm). In the downdraft stage ($t/T_0 = -1.8, -1.1$), the downward velocity is high near the front of the descending parcel (thermal cap). The local maximum appears always on the centerline and moves downward. The fluid underneath the thermal is pushed down, while the fluid at the side rises, forming a large-scale circulatory flow. Its center lies near the side boundary of the two fluids, and this structure continues to exist during the impinging stage ($t/T_0 = 1.9, 3.7$) and diverging stage ($t/T_0 = 5.6, 7.4$). Of particular importance is the alternating regions of upward and downward flow in the gust front associated with the circulatory flow. The downward flow remains significantly long after the high-density parcel has passed by. The circulatory flow structure shown here is similar to the laminar thermal, which was explained by Hill's vortex theory [17], as will be mentioned later.
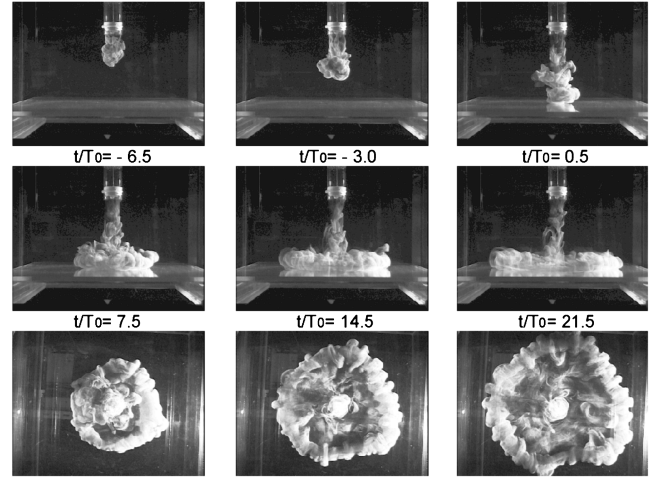
The contours of the radial component in Fig. 6 indicate abrupt increase close to the ground during the impinging stage. A local maximum appears there at this stage, as hypothesized by Fujita [1]
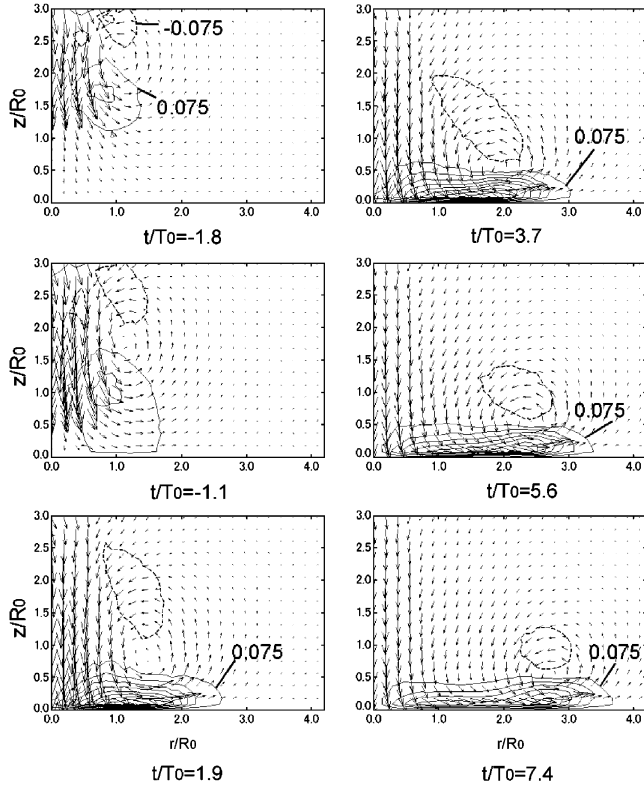
Fig. 6 Ensemble-averaged contours of radial velocity component V_r/V_0 together with velocity vector map ($Re = 2100$, contour interval is 0.075, solid and dotted lines indicate positive and negative values).
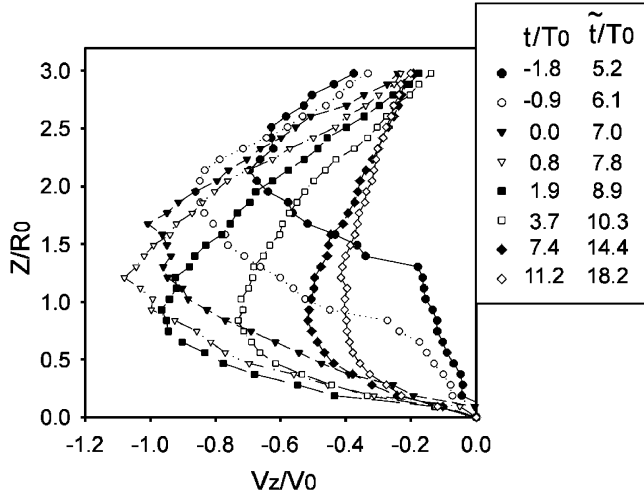

Fig. 7 Time change of vertical velocity profile along the centerline ($Re = 2100$, t is time elapsed from moment of impingement, $\tilde{t}$ is time from moment of burst of film).
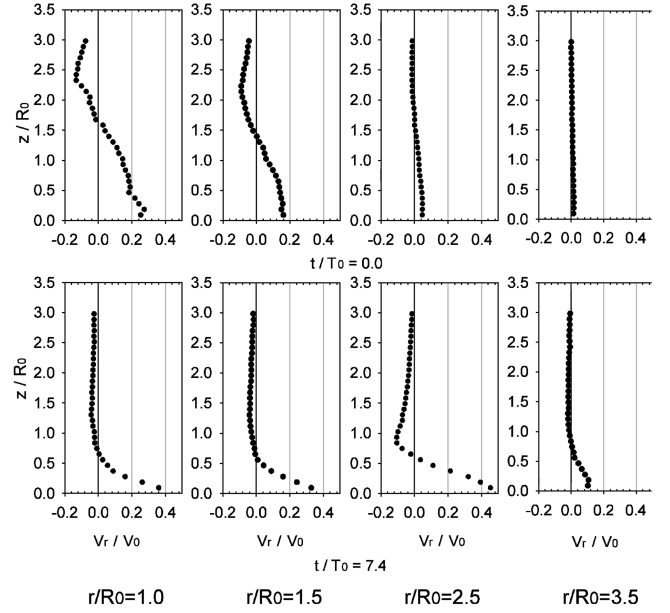

Fig. 8 Vertical distributions of V_r at different radial positions (upper: moment of impingement, lower: diverging stage, $Re = 2100$).
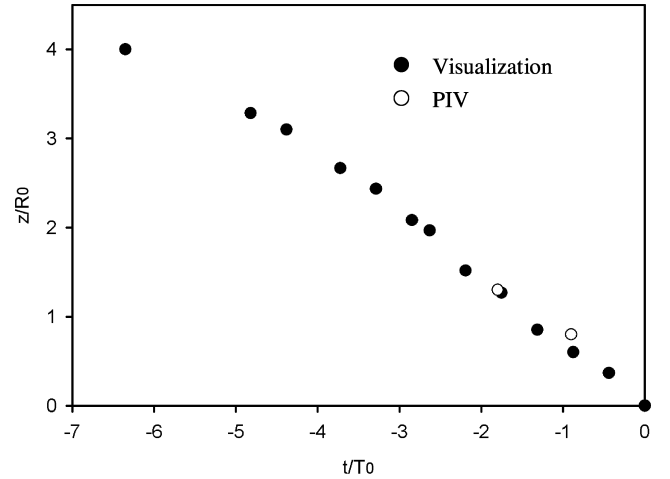

Fig. 9 Vertical position of the bottom of the descending parcel ($Re = 2100$).

and proven by a numerical simulation by Proctor [10]. Its radial position is located at some distance upstream of the center of the circulatory flow, similar to the instantaneous velocity field reported by Alahyari and Lundgren [8].

The time variation of the V_z profile along the vertical centerline is given in Fig. 7. Shortly after release ($\tilde{t} = 5.2T_0$ and $6.1T_0$), the velocity profile exhibits two parts with a kink. The visualization images suggest that the upper part corresponds to the main body of the high-density parcel, while the lower part corresponds to the low-density fluid pushed down by it. Since the latter disappears at $\tilde{t} = 7.0T_0$, we define this instant as the moment of impingement. The local maximum of the downward velocity gradually increases during the downdraft stage ($t < 0$) and reaches its maximum of $|V_z| \approx 1.1V_0$

at $t = 0.8T_0$, just after impingement. It then decreases rapidly, but the peak position stays at nearly the same height, $z \approx 0.8R_0$.

In Fig. 8, the vertical distributions of radial velocity component V_r at different radial positions are shown. At the moment of impingement (upper), the radial component has already grown significantly at the inner radial positions ($r \leq 1.5R_0$). At $t = 7.4T_0$ (diverging stage), the region of radially outward flow lies near the ground and has nearly constant thickness ($\approx 0.6R_0$). An unsteady boundary layer is supposed to develop during the diverging stage, but it lies mostly outside the region of measurement, and its outer edge is only just observed at the outermost profile ($r = 3.5R_0$) at this moment. The peak radial velocity amounts to $0.71V_0$ at $1.9 \leq t/T_0 \leq 3.6$, $1.2 \leq r/R_0 \leq 1.7$ and $z/R_0 \approx 0.1$.

The vertical position of the bottom of the descending parcel is plotted against time in Fig. 9. The result estimated from the ensemble-averaged velocity coincides well with the visual result. The average speed is $0.57V_0$, although it is slightly high.

C. Characteristics of Circulatory Flow

Downbursts have long been considered in relation to vortex rings [1,5]. Wilson, et al. [5] reported three dimensionality of a gust front, which may be interpreted as the azimuthal instability of a vortex ring.
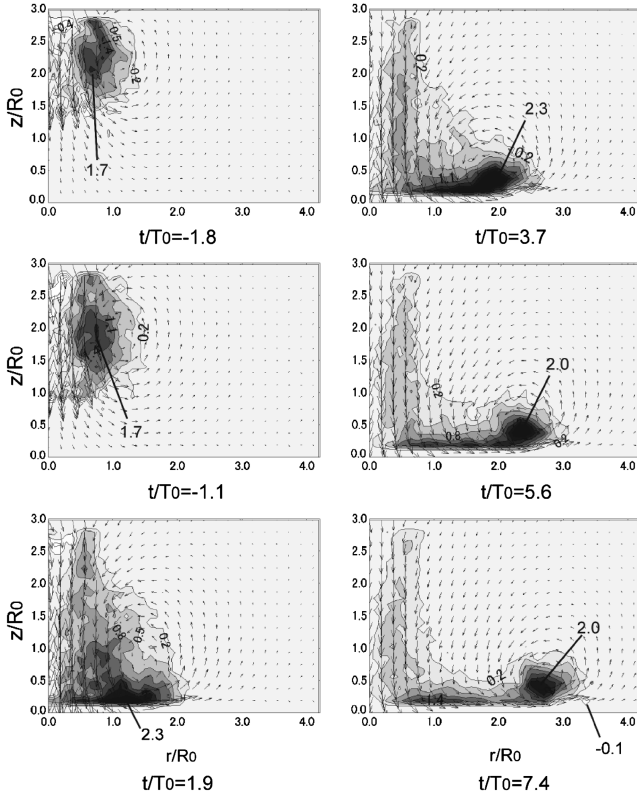
Fig. 10 Azimuthal component of ensemble-averaged vorticity $\omega_\theta R_0/V_0$ ($Re = 2100$), (contour interval is 0.3).

Fig. 11 Ensemble-averaged circulatory flow pattern (vector maps) and streamlines predicted using Hill's spherical vortex theory (solid lines) ($t/T_0 = -0.7$).

However, the characteristics and origin of the circulatory flow associated with a downburst is not yet clear.

As seen in Figs. 5 and 6, the circulatory flow pattern is marked in the ensemble-averaged velocity vector maps. In the downdraft stage, this region extends far beyond the thermal both in radial and vertical directions. Alahyari and Lundgren [8] found a similar flow pattern in their instantaneous images and interpreted it to be a vortex ring caused by the roll-up of the shear layer between two fluids. Figure 10 shows the azimuthal component of ensemble-averaged vorticity,

$$\omega_\theta = \frac{\partial V_r}{\partial z} - \frac{\partial V_z}{\partial r} \qquad (3)$$

which is evaluated by differentiation of fourth-order polynomials fitted to the ensemble-averaged velocity components. In the downdraft stage ($t/T_0 = -1.8, -1.1$), the region of high vorticity lies near the side boundary of the descending parcel, but the peak position does not coincide with the center of the circulatory flow, and the outer part of the circulatory flow is wholly irrotational. The region of high vorticity becomes closer to the ground ($t/T_0 = +1.9$), while the center of the circulatory pattern is located far above. During impingement, a new negative peak appears close to the ground. It moves radially outward and is gradually caught up into the circulatory flow and is eventually grows into a vortex ring with concentrated vorticity at its center.

According to Houze [18], this circulatory pattern may be interpreted as an inviscid flow driven by the buoyancy pressure-gradient force around a uniformly buoyant parcel of finite dimensions. Neglecting viscosity and taking the divergence of Eq. (1) and using the continuity equation, the following equation for pressure can be obtained.

$$\nabla^2 (p - p_0) = -g \frac{\partial}{\partial z}(\rho - \rho_0) - \nabla \cdot \{\rho_0 (\boldsymbol{u} \cdot \nabla)\boldsymbol{u}\} \qquad (4)$$

This equation suggests that the pressure perturbation can be divided into two parts, the buoyancy-driven pressure field p_B and the dynamically driven pressure field. Then p_B must satisfy
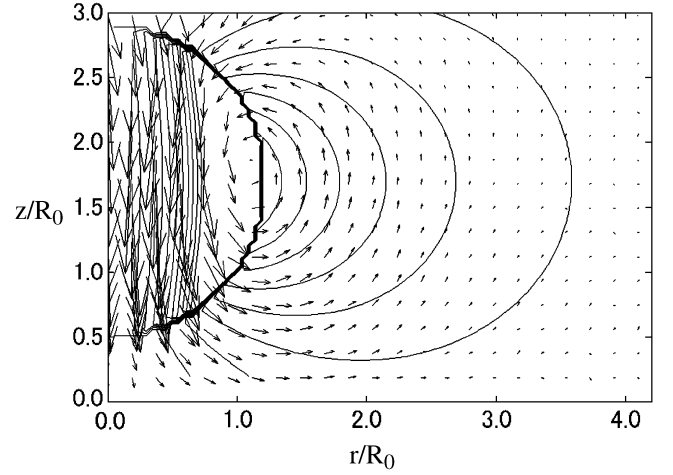
$$\nabla^2 p_B = -g \frac{\partial}{\partial z}(\rho - \rho_0) \qquad (5)$$

This is analogous to the electrostatic equation and the solution exhibits well-known electrostatic potential lines starting from the bottom of the parcel and returning to the top.

Another interpretation is possible if we imagine the streamlines around a downward moving solid body seen from a stationary observer. A quantitative explanation was given by Turner [17]. He attempted to interpret streamlines inside a thermal using Hill's spherical vortex theory, in which vorticity is confined within the spherical region and the flow outside is irrotational. According to this theory, the stream function is given by

$$\psi = \begin{cases} \frac{-C}{10}\left(r^4 + r^2 z^2 + \frac{5}{3} r^2 a^2\right) & \text{for } r^2 + z^2 < a^2 \\ \frac{Cr^2 a^5}{15(r^2 + z^2)^{3/2}} & \text{for } r^2 + z^2 > a^2 \end{cases} \qquad (6)$$

The resulting streamlines correspond to those around a solid sphere of radius a and moving in a stationary fluid with velocity equal to $2Ca^2/15$ [19]. The streamlines are obtained by setting $a = R_0$ and are illustrated by the solid lines in Fig. 11. When compared with the measured ensemble-averaged velocity vector map obtained at $t/T_0 = -0.7$, the agreement is quite obvious, particularly outside the descending parcel. Slight disagreement near the ground may be due to the ground effect, which is ignored in the Hill's theory.

The above observations tell us that this average circulatory flow is essentially irrotational, at least in the initial stage of development. During the diverging stage, the high shear layer near the ground is gradually caught up into the circulatory flow pattern and eventually grows into a vortex ring with concentrated vorticity at its center. In addition, the instantaneous flow field shows several closed streamlines with concentrated vorticity. Although this suggests the roll-up of the shear layer as hitherto believed [8], the instantaneous closed streamlines disappear during the ensemble average due to randomness, leaving only the vorticity due to the background shear.

D. Apparent Reynolds Stresses

Turbulence statistics are also important to improve the numerical prediction, as well as to construct a turbulence model in gravitational flow. The key points are the turbulence generation by the mean shear and buoyancy, and effects of the abrupt change of flow direction during impingement.

Contour maps of apparent Reynolds stress components together with velocity vector maps are given in Figs. 12–14. In the present method of downdraft generation, the magnitude of the initial disturbance is finite and of moderate reproducibility. Furthermore, the time from release is insufficient for the flow to forget the initial condition, at least in the initial stage. Thus the measured correlation
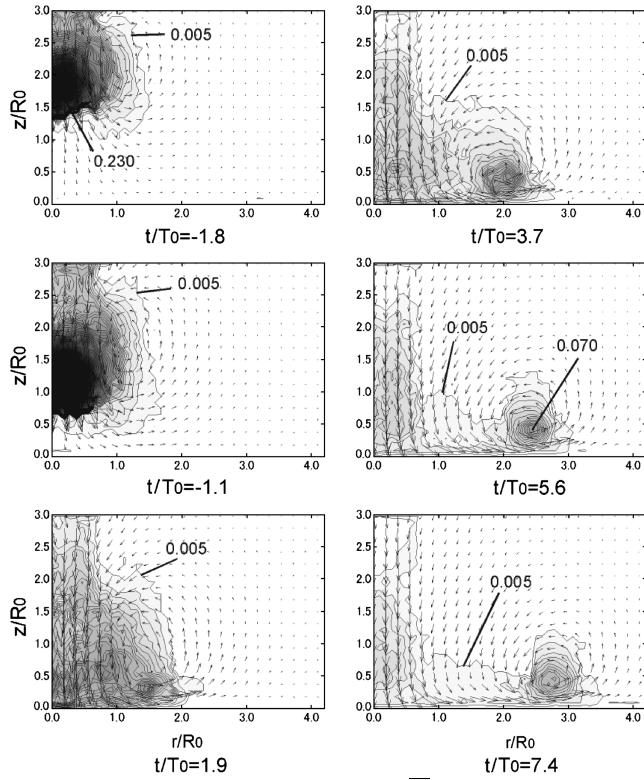
Fig. 12   Apparent Reynolds normal stress $\overline{v_z^2}/V_0^2$ (contour interval is 0.005).

Fig. 14   Apparent Reynolds shear stress $\overline{v_r v_z}/V_0^2$ (contour interval is 0.005, dotted lines indicate negative values).

$$P_{zz} \equiv -2\rho_0\left(\overline{v_z^2}\frac{\partial V_z}{\partial z} + \overline{v_z v_r}\frac{\partial V_z}{\partial r}\right) \tag{7a}$$

$$P_{rr} \equiv -2\rho_0\left(\overline{v_r^2}\frac{\partial V_r}{\partial r} + \overline{v_z v_r}\frac{\partial V_r}{\partial z}\right) \tag{7b}$$

$$P_{rz} \equiv -\rho_0\left(\overline{v_z^2}\frac{\partial V_z}{\partial z} + \overline{v_r^2}\frac{\partial V_z}{\partial r} - \overline{v_z v_r}\frac{V_r}{r}\right) \tag{7c}$$

are evaluated and plotted in Fig. 15.

As seen in Fig. 12, in the downdraft stage ($t/T_0 = -1.8, -1.1$), the vertical component $\overline{v_z^2}$ is confined within the high-density parcel, particularly in the front part. Although not shown here, it attains a maximum of $\overline{v_z^2} \approx 0.3V_0^2$ at $t = -0.2T_0$ just before impingement. Then it decays rapidly during impingement, leaving a discrete region of large $\overline{v_z^2}$ at the front of the diverging flow. The region of large P_{zz} shown in Fig. 15 mostly coincides with that of the stress itself.

$\overline{v_r^2}$ (Fig. 13) is much smaller than the vertical component in the downdraft stage and slightly higher in the side shear region than at the center of the downdraft column. During impingement ($t/T_0 = +1.9$), it increases rapidly near the ground and reaches its maximum of $0.1V_0^2$. Then it decays, leaving a high value within the gust front. P_{rr} (Fig. 16) is most pronounced close to the ground during impingement where the mean flow turns from vertical to horizontal. The region of high apparent shear stress $\overline{v_r v_z}$ (Fig. 14) approximately coincides with that of normal stress. During the downdraft stage, P_{rz} (Fig. 17) is large in the side shear region. During impingement, high production occurs in the same region as P_{rr}, while it is disclosed in front of diverging flow. Figure 18 shows turbulent energy evaluated from

$$k = \frac{3}{4}\left(\overline{v_r^2} + \overline{v_z^2}\right) \tag{8}$$

A high-energy region is found at the bottom of high-density parcel during the downdraft stage, close to the ground during impingement, and at the gust front during diverging stage.
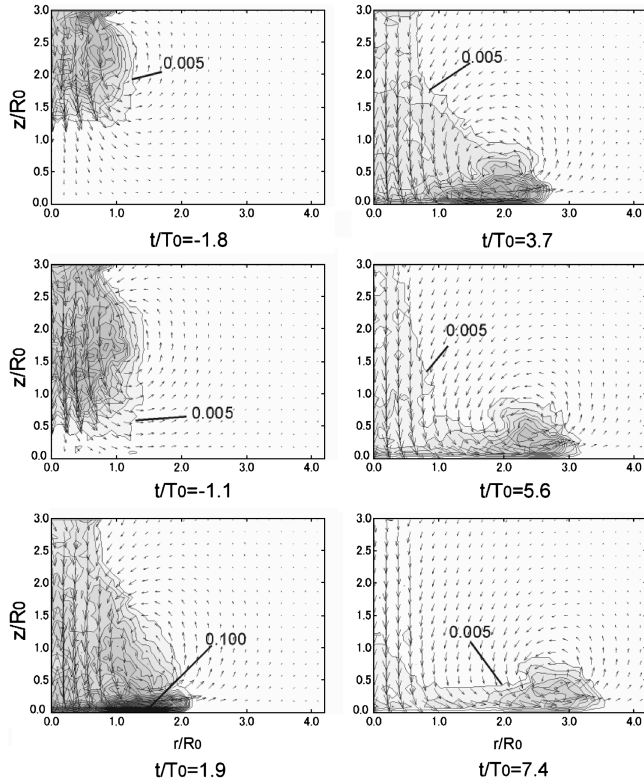

Fig. 13   Apparent Reynolds normal stress $\overline{v_r^2}/V_0^2$ (contour interval is 0.005).

should not be simply interpreted as Reynolds stress caused by the turbulence dynamics, but is better understood as the deviation of velocity from the ensemble average, which partially reflects the turbulence activity such as generation by shear. For comparison, the stress production terms by mean shear,
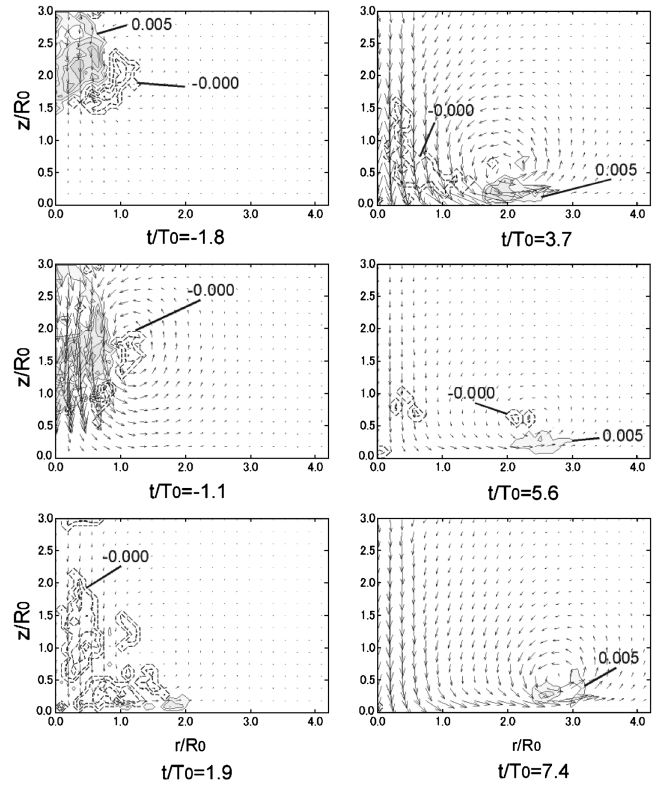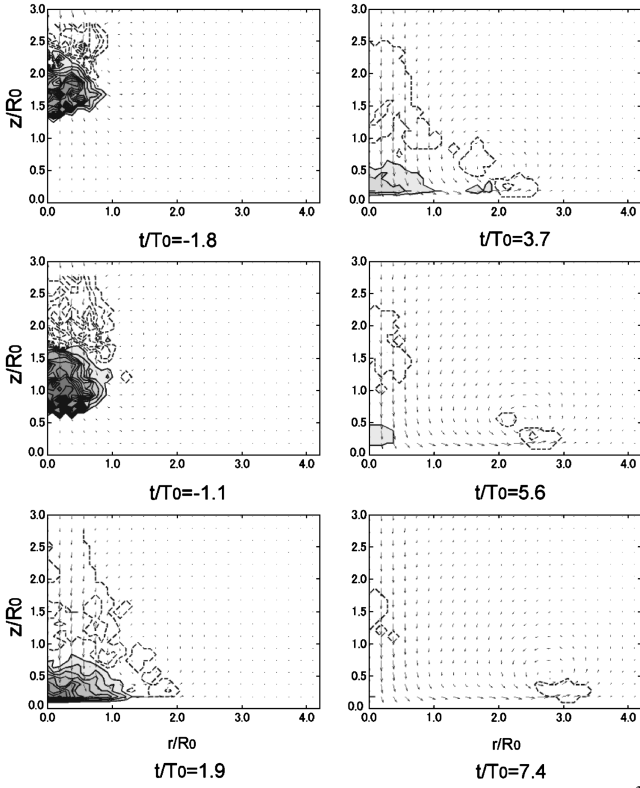
Fig. 15 Production of Reynolds normal stress by mean shear $P_{zz}R_0/V_0^3$ (contour interval is 0.03, dotted lines indicate negative values).
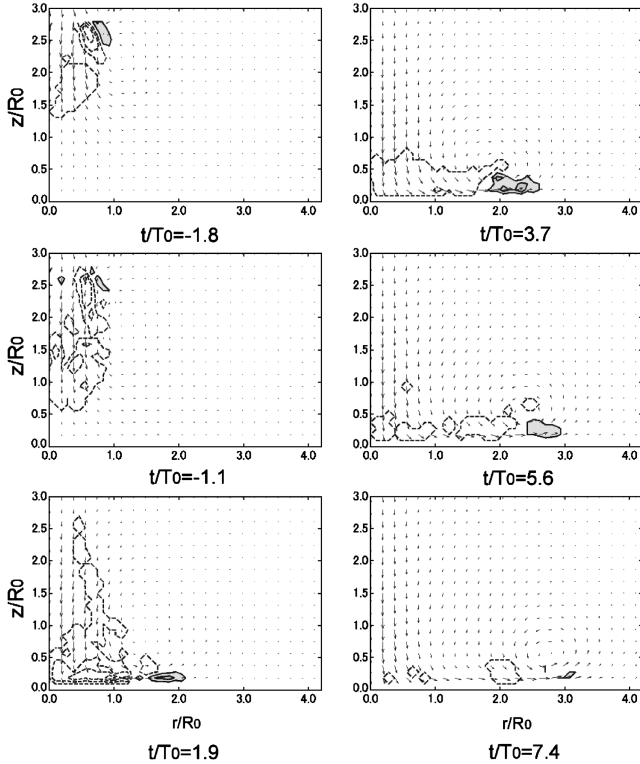

Fig. 16 Production of Reynolds normal stress by mean shear $P_{rr}R_0/V_0^3$ (contour interval is 0.03, dotted lines indicate negative values).
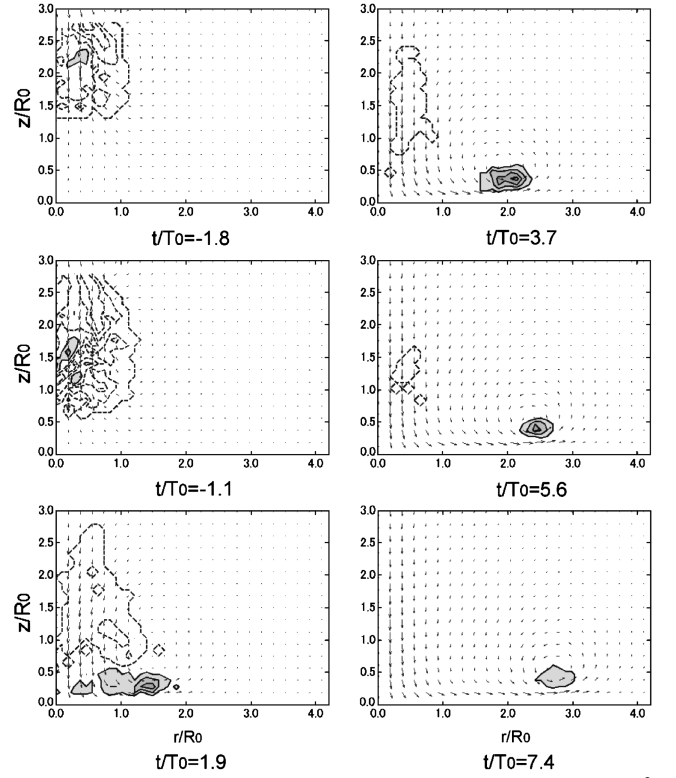

Fig. 17 Production of Reynolds shear stress by mean shear $P_{rz}R_0/V_0^3$ (contour interval is 0.03, dotted lines indicate negative values).

The coincidence between stress components and corresponding production rates indicates that the present stress field is not significantly contaminated by jitter, but reflects the turbulence - producing activity of mean shear. In addition to shear production, the present turbulent field might be affected by the extra production by buoyancy $(-2g\overline{\rho' v_z}/\rho_0, 0. - g\overline{\rho' v_r}/\rho_0)$ for $(\overline{v_z^2}, \overline{v_r^2}, \overline{v_r v_z})$, although

such contributions cannot be estimated before the information on the fluctuating density field is provided.

IV. Comparisons and Applications

A. Comparison with Existing Data

The results of the present laboratory experiment are now compared with the previous results including the data sets of real downbursts. Case A is the average over 70 downbursts observed by JAWS [5,6] while case B is a single downburst observed on 30 June, 1982, in Denver, Colorado [5]. Case C is the numerical simulation by Proctor [10], and case D is the laboratory experiment by Alahyari et al. [8]. In the comparison of the laboratory results with the real atmosphere, the most serious problem is the huge difference in the length scales. If we define Reynolds numbers on the basis of molecular viscosity, they differ by the order of 10^7. To overcome this difficulty, it is usually assumed that the viscosity for large-scale motion of the Earth's atmosphere is not caused by molecular motion but by the motion of turbulent eddies. Even in this case, the eddy viscosity in the atmosphere is neither uniform nor isotropic and one should accept crude assumptions. In the present comparison, the eddy viscosity of the real atmosphere is assumed to be 10 m^2/s, which is the accepted value of the mean vertical component. Another problem is how to estimate the length and time scales in a real downburst. Instead of the radius of an equivalent sphere R_0, R_D is chosen as the length scale because it is available both in the atmosphere and in the laboratory. According to Alahyari's idea [8], the time scale for the real downburst is estimated from the simplified form of the momentum equation,

$$\frac{Dv_z}{Dt} \approx -\frac{\rho - \rho_0}{\rho_0}g \qquad (9)$$

Using the maximum value of observed downward acceleration for the left-hand side, the density difference is estimated, and then the time scale is evaluated from Eq. (2).

The results are given in Table 1. Comparison of the results of the present model with the average value of the real downbursts (case A) reveals that the maximum values and positions of vertical and radial
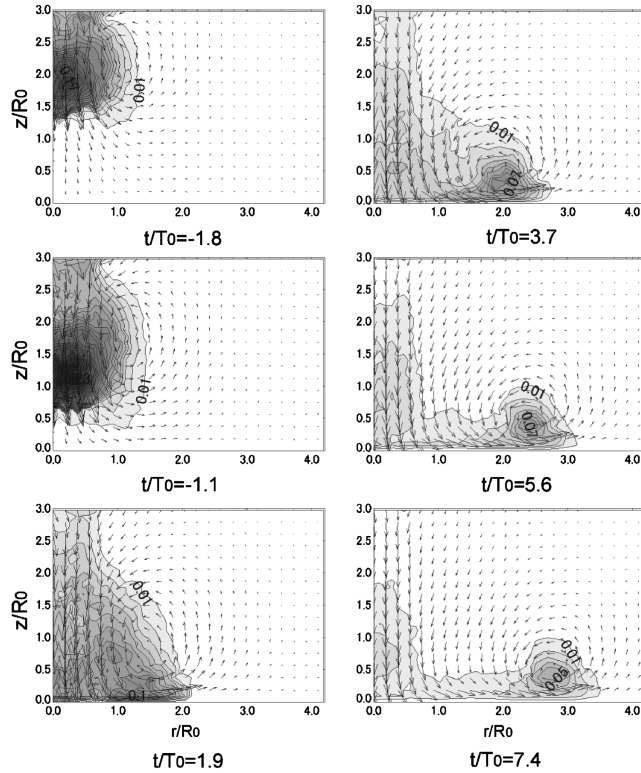
Fig. 18 Turbulent energy distribution k/V_0^2 (contour interval is 0.01).
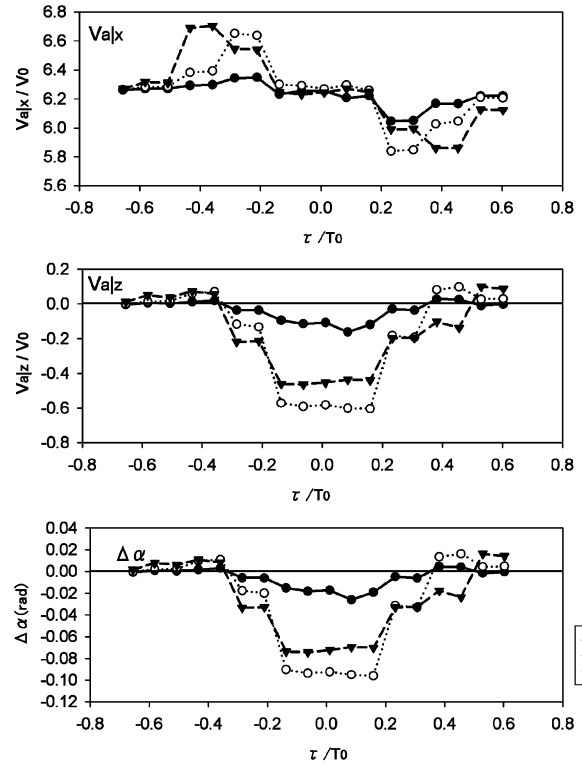

Fig. 19 Time history of airspeed and attack angle during an encounter with a typical downburst: a) horizontal component, b) vertical component, c) attack angle, ground speed $V_g = 75$ m/s ($0.625V_0$), attitude is 300 m.

velocities, as well as the thickness of the diverging flow, are in reasonable agreement. The other three cases are instantaneous results and comparison with the averaged data does not make too much sense. Keeping this in mind, it is recognized that the agreement between the instantaneous data and present results of the maximum of the vertical velocity and the radial position of maximum radial velocity are acceptable, while the maximum radial velocity is too large and the thickness of diverging flow is too small in the instantaneous cases.

B. Application to Aircraft Safety

As shown above, the present laboratory model is of reasonable quality for application to the aircraft safety issue. The most important information for an aircraft flying across a downburst is the time variation of the airspeed vector relative to the aircraft. Let us consider an aircraft flying horizontally into a region of a typical downburst along the diameter at altitude h with constant V_g and angle of attack α_0. Representing the velocity field of the downburst as $V(x, z, t)$, where $|x| = r$, V_a relative to the aircraft can be expressed as

$$V_a(\tau) = V(V_g|\tau|, h, t_0 + \tau) - V_g i \qquad (10)$$

where t_0 denotes the crossing time, that is the absolute time at which the aircraft reaches the center of the downdraft column. τ is the time from this instant. i denotes a unit vector in the direction of flight path x. Then the change of attack angle $\Delta\alpha$ at an instant is expressed as

$$\Delta\alpha = \tan^{-1}\frac{V_a|_z}{V_a|_x} \qquad (11)$$

As an example, taking $V_g = 75$ m/s(270 km/h) and $h = 300$ m, which are typical values for an airliner approaching a runway, the time variations of airspeed and attack angle experienced by the aircraft are evaluated and shown in Fig. 19 for three typical crossing time t_0. Suppose that an aircraft passes through the center of a downdraft column during downdraft stage $t_0/T_0 = -1.1$, then the horizontal component exhibits a slight increase before the aircraft crosses the center and significant decrease later ($\tau > 0.15T_0$). The

Table 1 Present results and real downburst data obtained by atmospheric observations, as well as results of numerical simulation and other laboratory simulations[a]

	Present laboratory model	Case A (atmospheric data, average) [5,6]	Case B (atmospheric data, instantaneous) [5,6]	Case C (numerical simulation) [10]	Case D (laboratory simulation) [8]
Re	2100	1200	1210	1210	3600
Maximum downward velocity $V_{z\,\mathrm{max}}$	1.1 0.23	1.0	1.6	1.3	2.5
Vertical position of $V_{z\,\mathrm{max}}$	1.2	1.5			
Maximum of radial velocity $V_{r\,\mathrm{max}}$	0.7 0.23	1.0	1.8	2.3	3.1
Radial position of $V_{r\,\mathrm{max}}$	1.2	1.6	1.4	1.2	1.2
Vertical position of $V_{r\,\mathrm{max}}$	0.1	0.08			
Thickness of diverging flow	1.0	0.7	0.23 0.54	0.16 0.38	
Lifetime		11			

[a]Reference length: radius of downdraft column. Reference time: estimated from Eqs. (2) and (9).

vertical component decreases slightly during transit across the center. The corresponding variation of the attack angle is rather mild and amounts to -1.5 deg. This results in a lift decrease of only 2% for the NACA66-210 aerofoil approaching at $\alpha = 4$ deg, for example. On the contrary, if the aircraft passes the center during impingement, $t_0/T_0 = +0.8$ for example, it experiences a sudden increase and decrease of horizontal components before and after the center crossing, respectively, and strong downward velocity during transit. The corresponding change of attack angle $\Delta\alpha$ is $+0.9$ deg at the gust front. This value is not large but it may be dangerous if the aircraft is approaching a runway at a high angle of attack close to the

stall angle. During transit, the attack angle suddenly decreases by more than -5.5 deg. The NACA66-210 aerofoil, for instance, approaching with $\alpha = 4$ deg completely loses lift. After impingement, $t_0/T_0 = +3.7$ for example, significant variation of airspeed still persists because of long-lasting downward flow following the main body of the descending parcel, as decribed in Sec. III.A.

For a wind shear hazard index of an aircraft encountering an abrupt change of magnitude and direction of wind, Bowles [20,21] proposed the F factor defined as

$$F \equiv \frac{1}{g}\frac{DV_x}{Dt} - \frac{V_z}{V_a}, \quad (12)$$

where V_a is the airspeed, V_x is the component of atmospheric wind directed horizontally along the flight path (positive for tail wind), and V_z is the vertical component (positive for upward wind). This relation is approximated as

$$F = \frac{V_g}{g}\frac{\partial V_x}{\partial x} - \frac{V_z}{V_a} \quad (13)$$

and evaluated using the present data, and contour plots are given in Fig. 20. The arrow on the upper margin indicates the aircraft ground speed and direction. For accelerating wind in the direction of flight path ($\partial V_x/\partial x > 0$) or for a descending air mass ($V_z < 0$), the F factor tends to be positive and the aircraft total energy is reduced due to wind shear. As seen in these figures, the region of a positive large F factor is always concentrated in the central region and contours are mostly symmetric. The large-scale circulatory flow does not contribute greatly to the F factor except at the gust front where the local updraft makes it negative. These findings indicate that the effect of the vertical component of airflow [second term on the right-hand side of Eq. (13)] is of primary importance. The maximum value reaches 0.13 at $t/T_0 = 1.1$, just after impingement, and then decreases gradually during the diverging stage.

Figure 21 is an example of time variations of the F factor experienced by an aircraft passing through the downburst region along the diameter. Altitude and ground speed are assumed to be $z/R_0 = 0.278$ and $V_g = 6.25V_0$. t_0 is the time of passage of the aircraft through the center measured from the time of impingement. If the aircraft reaches the center at $-0.46T_0$, that is, before impingement, it experiences a sudden increase up to $F = 0.08$, which is quickly followed by negative values. Such a small time-scale variation does not significantly change the flight trajectory. For $t_0 = 2.54T_0$, that is, the aircraft reaches the center during the impingement stage, the F factor reaches 0.11, and the aircraft is exposed to dangerous windshear for a longer period. For $t_0 = 6.24T_0$, that is, after impingement, the maximum F factor decreases to 0.08 but remains positive for a relatively long time. The
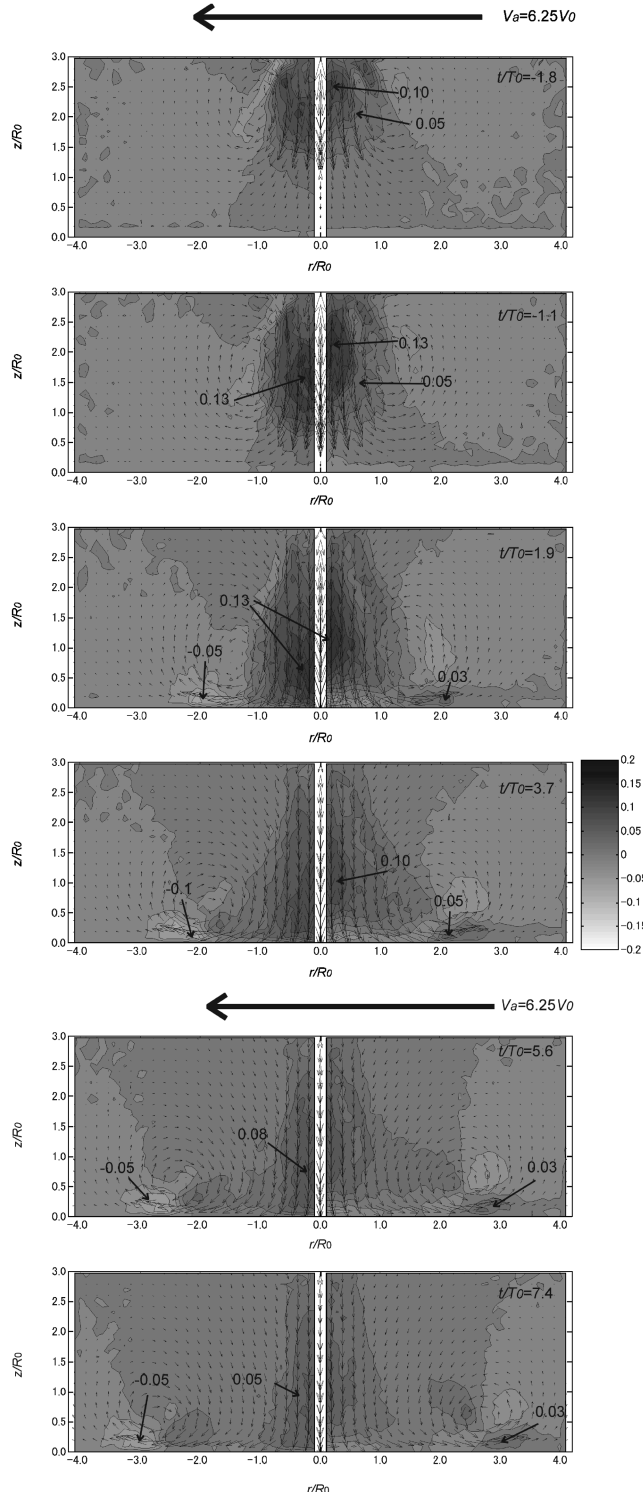

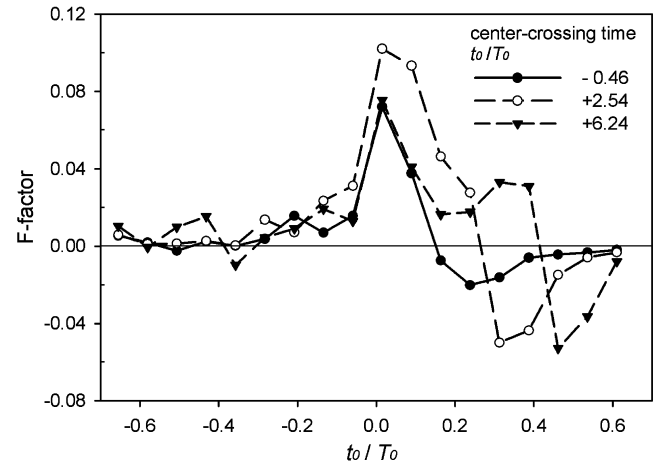Fig. 20 Distribution of F factor estimated from model data [ground speed $V_g = 6.25$ m/s (75 m/s)].

Fig. 21 Time variations of F factor experienced by an aircraft (attitude $z/R_0 = 0.278$, ground speed $V_g = 6.25V_0$, τ means time from center passage).

Federal Aviation Administration adopts a 1 km average of F factor greater than 0.1 as the windshear hazard threshold for a jet airliner. This 1 km average corresponds to the time average for $0.15T_0$ in our case. Since the mean value in the present model rarely exceeds this threshold, a large-scale jet aircraft may not suffer any crucial effect if it is properly controlled. However it is crucial for smaller low-speed aircraft because of the increasing significance of downward air velocity, as seen in the second term of the Eq. (13) as well as in Fig. 20.

V. Summary and Conclusions

As a laboratory model of downburst, the statistics of a velocity field of a vertical gravitational flow was investigated. By mechanically breaking a thin film placed at the bottom of a cylindrical container, a finite mass of a high-density liquid begins to fall into a stationary low-density liquid, forming a vertical thermal, that impinges onto the horizontal ground and diverges radially outward. By employing PIV, the ensemble-averaged maps of velocity vectors, azimuthal vorticity and turbulent stresses in a meridian plane were obtained. The statistical characteristics in the downdraft stage, impinging stage and diverging stage were examined and compared with the real downbursts observed in the atmosphere.

The large-scale circulatory flow was observed in the ensemble-averaged flow field. Before impingement, the closed streamlines start from the front of the high-density parcel, go upward at the side and return to the top. This flow is essentially irrotational and explained by Hill's spherical vortex theory. It grows during impingement, gathers up the vorticity generated close to the ground, eventually becomes a vortex ring with concentrated vorticity at its center and forms the nonaxisymmetric gust front. The downward velocity reaches the maximum of $1.1V_0$ just after impingement at the height of order R_0 and on the vertical centerline. The peak radial velocity amounts to $0.7V_0$ during impingement at $z/R_0 \approx 0.1$. High apparent Reynolds stress occurs within the main body of the high-density parcel. The production rate of vertical stress P_{zz} occurs near the front of it where the vertical shear is dominant, while that of radial component P_{rr} is large at the side during the downdraft stage and at the front of the diverging flow after impingement.

The results obtained by the present laboratory experiment are in reasonable agreement with the real observations if the molecular viscosity in the laboratory experiment is replaced by the vertical component of eddy diffusivity in the atmosphere, the length scale is defined as the radius of the downdraft column and the time scale of the real downburst is evaluated based on the simplified vertical momentum equation.

Finally, the F factor and the sudden change in the angle of attack were evaluated and the risk to an aircraft encountering a downburst was discussed referring to the results of the laboratory model. It was revealed that, in a typical case, the aircraft experiences sudden decrease of over 10 deg in the attack angle near the center of the downdraft column and loses more than 50% of lift. At the gust front, it experiences an angle increase on the order of 1 deg. This small increase cannot be ignored if the aircraft is approaching a runway with a high angle of attack near the limit of the stall margin.

Acknowledgment

References

[1] Fujita, T. T., *The Downburst*, University of Chicago Press, Chicago, IL, 1986, pp. 8, 9.

[2] Fujita, T. T., "Manual of Downburst Identification for NIMROD," SMRP Research Paper, No. 156, 1978.

[3] McCarthy, J., Roberts, R, and Schreiber, W., "JAWS Data Collection, Analysis Highlights and Microburst Statistics," *Proceedings of the 21th Radar Meteorological Conference*, 1983, pp. 596–601.

[4] Rinehart, R. E., and Isaminger, A., "Radar Characteristics of Microbursts in the Mid South," *Proceedings of the 23rd Radar Meteorological Conference*, 1986, pp. 71–76.

[5] Wilson, J. W., Roberts, R. D., Kessinger, C., and McCarthy, J., "Microburst Wind Structure and Evolution of Doppler Radar for Airport Wind Shear Detection," *Journal of Climate and Applied Meteorology*, Vol. 23, 1984, pp. 898–915.

[6] Hjelmfelt, M. R., "Structure and Life Cycle of Microburst Outflow Observed in Colorado," *Journal of Climate and Applied Meteorology*, Vol. 27, Aug. 1988, pp. 900–927.

[7] Lundgren, T. S., Yao, J., and Mansour, N. N., "Microburst Modeling and Scaling," *Journal of Fluid Mechanics*, Vol. 239, 1992, pp. 461–488.

[8] Alahyari, A., and Longmire, E. K., "Dynamics of Experimentally Simulated Microbursts," *AIAA Journal*, Vol. 33, No. 11, 1995, pp. 2128–2136.

[9] Srivastava, R. C., "A Simple Model of Evaporatively Driven Downdraft: Application to Microburst Downdraft," *Journal of the Atmospheric Sciences*, Vol. 45, No. 21, 1985, pp. 1004–1023.

[10] Proctor, F. H., "Numerical Simulation of an Isolated Microburst. Part 1: Dynamics and Structure," *Journal of the Atmospheric Sciences*, Vol. 45, No. 21, 1988, pp. 3137–3160.

[11] Droegemeier, K. K., and Wilhelmson, R. B., "Numerical Simulation of Thunderstorm Outflow Dynamics. Part 1: Outflow Sensitivity Experiments and Turbulence Dynamics," *Journal of the Atmospheric Sciences*, Vol. 44, No. 8, 1987, pp. 1180–1210.

[12] Anderson, J. R., Droegemeier, K. K., and Wilhelmson, R. B. "Simulation of the Thunderstorm Subcloud Environment," *Proceedings of the 14th Conference on Severe Local Storms*, 1985, pp. 147–150.

[13] Escudier, M. P., and Maxworthy, T., "On the Motion of Turbulent Thermals," *Journal of Fluid Mechanics*, Vol. 61, Pt. 3, 1973, pp. 541–552.

[14] Beghin, P., Hopfinger, E. J., and Britter, R. H., "Gravitational Convection from Instantaneous Sources on Inclined Boundaries," *Journal of Fluid Mechanics*, Vol. 107, 1981, pp. 407–422.

[15] Fukushima, Y., "Numerical Simulation of Gravity Current Front," *Journal of Hydraulic Engineering*, Vol. 124, No. 6, 1998, pp. 572–578.

[16] Widnall, S. E., Bliss, D., and Tsai, C. Y., "The Instability of Short Waves on a Vortex Ring," *Journal of Fluid Mechanics*, Vol. 66, Pt. 1, 1974, pp. 35–47.

[17] Turner, J. S., "The Flow into an Expanding Spherical Vortex," *Journal of Fluid Mechanics*, Vol. 18, 1964, pp. 195–208.

[18] Houze, R. A., Jr., *Cloud Dynamics*, Academic Press, New York, 1993, pp. 223–226.

[19] Saffman, P. G., *Vortex Dynamics*, Cambridge University Press, Cambridge, U.K., 1992, pp. 23–24.

[20] Bowles, R. L., "Windshear Detection and Avoidance—Airborne Systems Survey," *29th IEEE Conference on Decision and Control*, 1990, pp. 708–736.

[21] Bowles, R. L., "Reducing Windshear Risk through Airborne Systems Technology," *The 17th Congress of ICAS*, 1990, pp. 1603–1630.